Nonlinear Dynamics of a Jeffcott Rotor with Torsional Deformations and Rotor-Stator Contact

Nicholas Vlajic[a] , Alan R. Champneys[a] , Balakumar Balachandran[b]

[a]*Department of Engineering Mathematics, University of Bristol, Bristol, England*
[b]*Department of Mechanical Engineering, University of Maryland, College Park, USA*

Abstract

The dynamics of a modified Jeffcott rotor is studied, including rotor torsional deformation and rotor-stator contact. Conditions are studied under which the rotor undergoes either forward synchronous whirling or self-excited backward whirling motions with continuous stator contact. For forward whirling, the effect on the response is investigated for two commonly used rotor-stator friction models, namely, the simple Coulomb friction and a generalised Coulomb law with cubic dependence on the relative slip velocity. For cases with and without the rotor torsional degree of freedom, analytical estimates and numerical bifurcation analyses are used to map out regions in the space of drive speed and a friction parameter, where rotor-stator contact exists. The nature of the bifurcations in which stability is lost are highlighted. For forward synchronous whirling fold, Hopf, lift-off, and period-doubling bifurcations are encountered. Additionally, for backward whirling, regions of transitions from pure sticking to stick-slip oscillations are numerically delineated.

Keywords: Jeffcott rotor, bifurcations, drill-string dynamics, nonlinear oscillations, torsional vibrations

1. Introduction

The focus of this paper is on the dynamics of a modified version of the Jeffcott rotor [1], including the geometric nonlinearity originating from torsional-lateral coupling and friction due to rotor-stator contact. Such a rotor, which can undergo elastic torsional deformations in addition to the rigid body rotation about its drive axis has been studied previously, see [2] and the references within.

A key motivation for this simplified single-rotor model is its application in understanding the dynamics of rotary drill-strings, which are slender rotating structures that are used to drill for petrochemicals and in other geothermal applications. These structures are rather different from typical rotating machines, because they typically have large torsional deformations and can also feature significant imbalance and eccentricity originating from curvature in the string. Moreover, rotor-stator contact is often designed to be a key part of such devices through the introduction of stabilizing disks.

Previously, Edwards *et al.* [3] performed a parametric study of a rotor-stator system similar to the one presented here and mapped out regions of impacting motions and quasi-periodic behavior.

A main contribution of prior work [2] was the construction of a reduced-order model to show how the combined effects of lateral-torsional and nonlinear friction between the rotor and stator could create a Hopf instability during forward synchronous whirl with stator contact. Furthermore, an approximate analytic solution was derived in order to describe the torsional response during self-excited backward whirling vibrations for weakly nonlinear friction and for whirl speeds much greater than the uncoupled torsional natural frequency. Finally, the prior work [2] did not consider conditions under which loss of contact might occur.

Key questions remain as to how the approximate solutions presented in [2] map out into wider parameter regimes and to what extent the stability map is sensitively dependent on the choice of friction model. In this paper, the prior work in [2] is extended to answer these questions, via a mixture of analytical and numerical techniques. A more comprehensive study is performed to investigate the response of this rotor system during both forward and backward whirling with continuous stator contact. In particular, for typical sets of physical parameter values, we seek to map out the bifurcations that delineate regions of rotor-stator contact, synchronous forward whirl, self-excited backward whirl, and torsional oscillations with contact.

The work presented here is similar in spirit to the stability analysis performed by Mihajlovic *et al.* [4] who used experiments and a numerical model of a rotating shaft that is able to undergo torsional motions, but is constrained laterally. There, all of the nonlinear phenomena originated from the specific forms of the set-valued or velocity-weakening friction models, rather than through geometric effects. In a follow study [5], the same authors extended this model to include lateral deformations, but in which forces were assumed to be of follower-type and to act on the rotor for all lateral displacements. By contrast, in the model presented in Section 2 below, the authors do not make any such geometric approximations.

Using a similar model to the one presented here, it has been known at least since the work of Edwards *et al.* [3] that complex nonlinear motions can occur. In particular, they were able to map out parameter regions of impacting motion and quasi-periodic behavior.

It should however be noted that lateral-torsional coupling is not a necessary ingredient for rotor systems to exhibit impacting, aperiodic, or chaotic motions; see for example [6, 7]. Several studies, including those by [8, 9], have been devoted to investigating the onset and mechanism of self-excited backward whirl. Yet few studies [2, 10–12] have included torsional during analysis of backward whirling motions. Also, we are not aware of any previous presentation of a fundamental diagram showing the existence regions of synchronous forward whirl (cf. Fig. 3 below), even in the absence of torsional effects.

The rest of this paper is outlined as follows. In Section 2, the governing equations of motions, which were originally derived in [2], are presented here for completeness. Section 3 contains computations of existence and stability regions for the special case where there is no coupling between lateral and torsional motions. The cases of forward and backward whirl are considered seperately. In Section 4, the additional effects induced by torsional coupling are pointed out. Finally, Section 5 includes concluding remarks.

2. Rotor Equations of Motion and External Stator Forces

2.1. Derivation of Equations of Motion

A schematic of the Jeffcott rotor-stator system capable of torsional vibrations is shown in Figure 1(a). The rotor with radius R and mass M coincides with the center of the stator with a clearance δ in the static configuration. The rotor has a mass imbalance m with eccentricity e.

The quantity J_o is the mass moment of inertia of the rotor without mass imbalance about the z-axis. The rotor is assumed to be symmetrical so that the lateral stiffnesses have equivalent spring constants $k_x = k_y = k_b$, and has a torsional stiffness k. Similarly, the rotor has lateral damping that is assumed to be symmetric so that the equivalent damping coefficients are $c_x = c_y = c_b$. Torsional motions also experience dissipation denoted by the damping coefficient c. A schematic of the rotor in a dynamic state at an instant of time is depicted in Figure 1(b). The geometric center of the planar rotor is fully described in an inertial frame with coordinates x and y projected onto orthogonal unit vectors $\mathbf{a_1}$ and $\mathbf{a_2}$, respectively. Further, two sets of unit vectors, namely $\mathbf{b_1}$,$\mathbf{b_2}$ and $\mathbf{c_1}$,$\mathbf{c_2}$, are placed at the geometric center of the rotor.

The $\mathbf{b_1}$-$\mathbf{b_2}$ set rotates at a constant angular speed Ω with respect to the $\mathbf{a_1}$-$\mathbf{a_2}$ set. Thus, the angle between $\mathbf{a_1}$ and $\mathbf{b_1}$ is a measure of the rigid body rotation which we assume to be equal to Ωt, where Ω is an applied external drive frequency.

The mutually orthogonal unit vectors $\mathbf{c_1}$ and $\mathbf{c_2}$ are fixed to the rotor, and the angle between $\mathbf{b_1}$ and $\mathbf{c_1}$ is the torsional deformation given by θ. For notational convenience, let

$$\beta(t) \equiv \beta = \theta(t) + \Omega t,$$

which represents the superposition of the torsional deformation and rigid body rotation. Physically, the torsional stiffness k and damping c act to align the $\mathbf{b_1}$,$\mathbf{b_2}$ and $\mathbf{c_1}$,$\mathbf{c_2}$ unit vectors.

Additionally, the rotor is assumed to be only able to undergo planar motions with no out of plane motions due to rotations about the x and y axes. This constraint is imposed by defining $\mathbf{a_3} \equiv \mathbf{b_3} \equiv \mathbf{c_3}$ for all time t, where $\mathbf{a_3} \equiv \mathbf{a_1} \times \mathbf{a_2}$, $\mathbf{b_3} \equiv \mathbf{b_1} \times \mathbf{b_2}$ and $\mathbf{c_3} \equiv \mathbf{c_1} \times \mathbf{c_2}$. For convenience, at time $t = 0$, we suppose that $\mathbf{a_1} \equiv \mathbf{b_1} \equiv \mathbf{c_1}$, $\mathbf{a_2} \equiv \mathbf{b_2} \equiv \mathbf{c_2}$ and the mass imbalance m is located along the x-axis.

Under these assumptions, the equations of motion can readily be obtained by using Lagrangian mechanics, see [2] for details:

$$(M+m)\ddot{\bar{x}} + c_b\dot{\bar{x}} + k_b\bar{x} = me\left[\ddot{\beta}\sin\beta + \dot{\beta}^2\cos\beta\right] + \bar{F}_x, \tag{1}$$

$$(M+m)\ddot{\bar{y}} + c_b\dot{\bar{y}} + k_b\bar{y} = me\left[-\ddot{\beta}\cos\beta + \dot{\beta}^2\sin\beta\right] + \bar{F}_y, \tag{2}$$

$$J\ddot{\theta} + c\dot{\theta} + k\theta = me\left[\ddot{\bar{x}}\sin\beta - \ddot{\bar{y}}\cos\beta\right] + \bar{M}_t, \tag{3}$$

in which $J = J_o + me^2$. For analysis (but not simulations, because of the polar singularity) it is useful to express the position of the rotor in polar coordinates. In light of this, Eqs. (1), (2), and (3) can be written in polar coordinates with the transformation

$$\bar{x} = \bar{\rho}\cos\gamma \tag{4a}$$

$$\bar{y} = \bar{\rho}\sin\gamma \tag{4b}$$

In Eqs. (4), $bar\rho \equiv \bar{\rho}(t)$ is the polar amplitude and $\gamma \equiv \gamma(t)$ is the angle between the position vector from the origin to the geometric center of the rotor and the x-axis. In practice, it is simpler to substitute Eqs. (4) into the kinetic energy, potential, and Raleigh's dissipation function given in [2] and use Lagrange's equations with generalized coordinates $\bar{\rho}$, $\bar{\gamma}$, and $\bar{\theta}$. Equations (1), (2), and (3) can then be re-written in polar coordinates as:

$$(M+m)\ddot{\bar{\rho}} - (M+m)\bar{\rho}\dot{\gamma}^2 + c_b\dot{\bar{\rho}} + k_b\bar{\rho} = me\left(\bar{\Omega} + \dot{\theta}\right)^2\cos\psi + me\ddot{\theta}\sin\psi - \bar{F}_n, \tag{5}$$

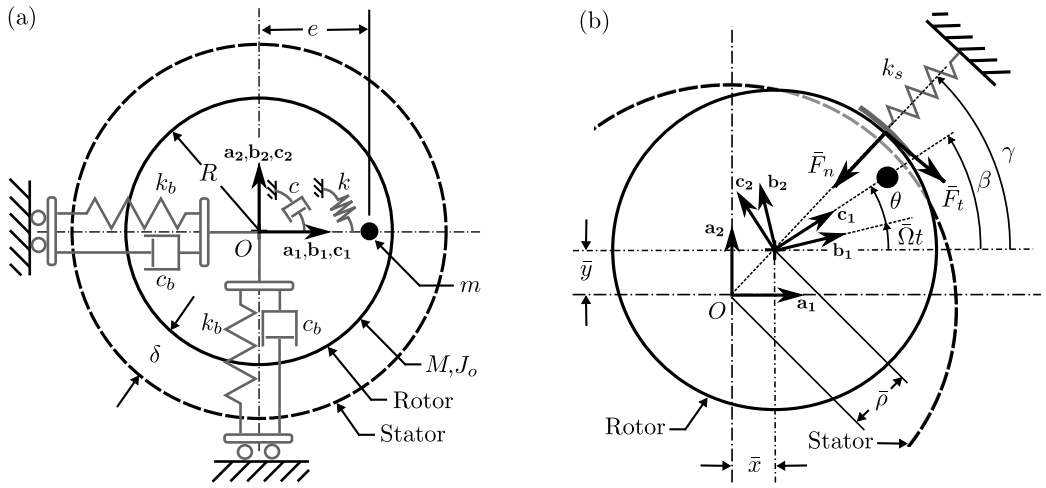

Figure 1: (a) Static configuration of the rotor within the stator. (b) Rotor system in a dynamic state, after [2].

$$(M+m)\bar{\rho}^2\ddot{\gamma} + 2(M+m)\bar{\rho}\dot{\bar{\rho}}\dot{\gamma} + c_b\bar{\rho}^2\dot{\gamma} = me\bar{\rho}\left(\bar{\Omega}+\dot{\theta}\right)^2\sin\psi - me\bar{\rho}\ddot{\theta}\cos\psi - \bar{\rho}\bar{F}_t, \tag{6}$$

$$J\ddot{\theta} + c\dot{\theta} + k\theta = -me\left(\bar{\rho}\dot{\gamma}^2 - \ddot{\bar{\rho}}\right)\sin\psi - me\left(2\dot{\bar{\rho}}\dot{\gamma} + \bar{\rho}\ddot{\gamma}\right)\cos\psi - \bar{M}_t, \tag{7}$$

where

$$\psi \equiv \psi(t) = \beta - \gamma = \bar{\Omega}t - \gamma + \theta. \tag{8}$$

2.2. Non-Dimensionalization

Equations (1), (2), and (3), as well as (5), (6), and (7) are nondimensionalized by introducing the following parameters:

$$\rho = \frac{\bar{\rho}}{\delta},\ \ x = \frac{\bar{x}}{\delta},\ \ y = \frac{\bar{y}}{\delta},\ \ \tau = t\omega_b,\ \ \Omega = \frac{\bar{\Omega}}{\omega_b},$$

$$\omega_b = \sqrt{\frac{k_b}{M+m}},\ \ \omega_t = \sqrt{\frac{k}{J}},\ \ 2\zeta_b = \frac{c_b}{\omega_b(M+m)},\ \ 2\zeta_t = \frac{c}{\omega_b J},$$

$$F_n = \frac{\bar{F}_n}{(M+m)\omega_b^2\delta},\ \ F_t = \frac{\bar{F}_t}{(M+m)\omega_b^2\delta},\ \ F_x = \frac{\bar{F}_x}{(M+m)\omega_b^2\delta},\ \ F_y = \frac{\bar{F}_y}{(M+m)\omega_b^2\delta},$$

$$M_t = \frac{\bar{M}_t}{J\omega_b} = m_f\mu F_n,\ \ m_f = \frac{(M+m)\delta R}{J},\ \ m_b = \frac{me}{(M+m)\delta},\ \ m_t = \frac{me\delta}{J}$$

Allowing superscript prime ()′ to denote the time derivative with respect to non-dimensional time τ, equations (1),(2), and (3) are transformed to:

$$x'' + 2\zeta_b x' + x = m_b\left[\beta''\sin\beta + \beta'^2\cos\beta\right] + F_x \tag{9}$$

$$y'' + 2\zeta_b y' + y = m_b \left[-\beta'' \cos\beta + \beta'^2 \sin\beta \right] + F_y \tag{10}$$

$$\theta'' + 2\zeta_t \theta' + \omega_t^2/\omega_b^2 \theta = m_t \left[x'' \sin\beta - y'' \cos\beta \right] + M_t \tag{11}$$

Similarly, equations (12), (13), and (14) are then rewritten:

$$\rho'' - \rho\gamma'^2 + 2\zeta_b \rho' + \rho = m_b(\Omega + \theta')^2 \cos\psi + m_b \theta'' \sin\psi - F_n \tag{12}$$

$$\rho^2\gamma'' + 2\rho\rho'\gamma' + 2\zeta_b \rho^2 \gamma' = m_b \rho(\Omega + \theta')^2 \sin\psi - m_b \rho\theta'' \cos\psi - \rho F_t \tag{13}$$

$$\theta'' + 2\zeta_t \theta' + \omega_t^2/\omega_b^2 \theta = -m_t(\rho\gamma'^2 - \rho'') \sin\psi - m_t(2\rho'\gamma' + \rho\gamma'') \cos\psi - M_t \tag{14}$$

2.3. External Stator Forces

Upon contact with the stator, the rotor is subject to a normal force that is assumed to be linearly proportional to the deflection of the stator with stiffness k_s. This may be written as

$$\bar{F}_n = \begin{cases} 0 & \text{for } \rho \le \delta \\ k_s(\rho - \delta) & \text{for } \rho > \delta \end{cases}, \tag{15}$$

where $k_s \gg 1$. The tangential force component is assumed to obey the usual principle of dry friction and is proportional to the normal force and a friction coefficient μ, via

$$\bar{F}_t = \mu \bar{F}_n.$$

The tangential and normal forces may be transformed to accommodate the external forces and moments in Eqs. (9),(10) and (11) by using the following geometric relations

$$\bar{F}_x = \frac{\bar{F}_t y - \bar{F}_n x}{\rho}, \quad \bar{F}_y = \frac{-\bar{F}_t x - \bar{F}_n y}{\rho}, \quad \bar{M}_t = \bar{F}_t R \quad \text{for } \bar{\rho} \neq 0 \tag{16}$$

2.4. Friction Models

The stability of the torsional vibrations and rotor response is studied for two different friction models. The coefficient of friction in both models is a function of relative speed between the the rotor and stator at the point of contact. From simple kinematics, the relative speed between the two surfaces at the point of contact is given to be:

$$\bar{v}_{\text{rel}} = (\Omega + \dot{\theta})R + \dot{\gamma}\rho = (\Omega + \dot{\theta})R - \dot{x}\frac{y}{\rho} + \dot{y}\frac{x}{\rho} \quad \text{for } \rho \neq 0. \tag{17}$$

It is noted that the relative speed v_{rel} is non-dimensionalized through the characteristic length and time parameters by $v_{\text{rel}} = \bar{v}_{\text{rel}}/(\delta\omega_b)$. The two friction models chosen here are Coulomb friction and velocity-weakening cubic. There are other friction models which account for certain physics on smaller length scales. However, these two models were chosen because of their qualitative behavior, which will be discussed next. The governing equations are given by

Coulomb:

$$\mu(v_{\text{rel}}) = \mu_o \text{sgn}(v_{\text{rel}}), \tag{18}$$

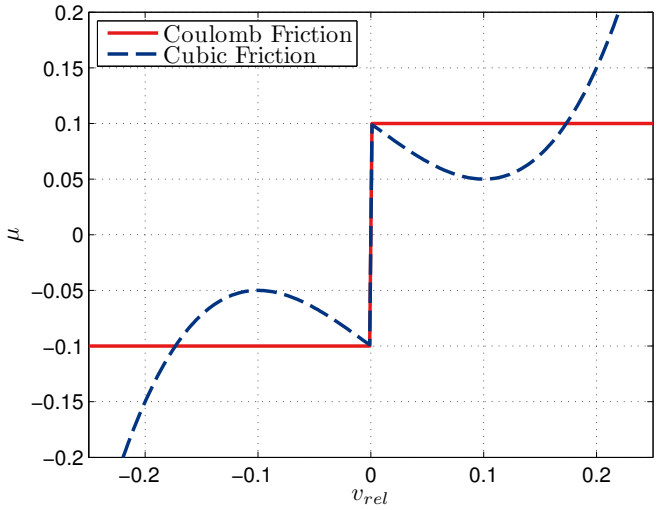

Figure 2: Coefficient of friction for Coulomb friction ($\mu_o = 0.1$) and cubic friction ($\mu_o = 0.1$, $v_m = 0.1$, $\mu_m = 0.05$) as a function of the relative speed.

Cubic:

$$\mu(v_{\text{rel}}) = \mu_o \text{sgn}(v_{\text{rel}}) - \mu_1 v_{\text{rel}} + \mu_3 v_{\text{rel}}^3, \tag{19}$$

where

$$\mu_1 = \frac{3}{2}\frac{\mu_o - \mu_m}{v_m}, \quad \mu_3 = \frac{1}{2}\frac{\mu_o - \mu_m}{v_m^3}.$$

Both friction models contain a set-value function when the relative speed between the two surfaces is zero. Thus, when $v_{\text{rel}} = 0, \mu(0) \in \{-\mu_o, \mu_o\}$ and μ can take on any set of values between $\pm\mu_o$. The models start to differ when the relative speed is away from zero. The Coulomb model provides a constant friction value for all values of v_{rel}. The cubic model has a negative slope near $v_{\text{rel}} \approx 0$, and has been referred to as velocity-weakening in the literature, and this feature effectively acts to capture the Stribeck effect.

In the cubic friction model, the friction coefficient reaches μ_m at a finite value of relative speed, namely, when $|v_{\text{rel}}| = |v_m|$. For values of $|v_{rel}| > |v_m|$, the slope of μ starts to increase. As will be shown later, these qualitative features have strong influence on the dynamics of the system.

In numerically integrating the governing equations, the signum function poses challenges. During the simulations, the signum function is approximated by the stiff normalized arctangent function

$$\text{sgn}(v_{\text{rel}}) \approx \frac{2}{\pi}\arctan(\delta_f v_{\text{rel}}), \tag{20}$$

In Eq. (20), the normalized arctangent function closely approximates the signum function for the smoothing parameter $\delta_f \gg 1$.

Throughout this work we use values of the fixed parameters given in Table 1. These values are similar to ones used in [2] and are representative of typical dimensionless values in which

Table 1: Parameter values used in simulations.

Parameter	Value	Units
ζ_b (c_b)	0.1 (0.2)	$N \cdot s/m$
ζ (c)	0.01 (3.0 e^{-4})	$N \cdot m \cdot s/rad$
e	0.05	m
M	0.9	kg
m	0.1	kg
k_b	1	N/m
k_s	$1e^4$	N/m
k	0.05	$N \cdot m/rad$
R	0.1	m
v_m	0.05-0.30	–
δ	0.01	m
δ_f	$1e^8$	-

the lateral natural frequency has been scaled to $\Omega = 1$. The uncoupled lateral natural frequency is on the same order as the uncoupled torsional natural frequency ($\omega_t/\omega_b \approx 3.2$), which is a characteristic trait of slender rotors. Moreover, this approximate ratio of natural frequencies between lateral and torsional motions is similar to the ratio of natural frequencies of the slender rotordynamic experiments presented in earlier work [11, 12].

3. Rotor-Stator Dynamics without Torsional Deformations

Within this section, torsional vibrations of the rotor-stator system are neglected (essentially by taking $k \to \infty$ and $\theta \equiv 0$), and parameter regions of rotor-stator contact are sought for the friction models presented in the previous section. For the analysis, the rotor is assumed to be in contact with the stator and parameter regions where the contact is broken are analytically and numerically determined. In the absence of torsional deformations, the rotor model reduces to the classical Jeffcott rotor contained within a stator.

3.1. Continuous Contact during Forward Synchronous Whirl

Forward synchronous whirl occurs when the rotor is permanently in contact with the stator in the slip state ($v_{\text{rel}} \neq 0$) and the angular displacement γ is completely synchronous with the drive rotation. In order to analyse the conditions under which such motion can occur it is useful to make the approximation of an infinitely stiff stator; that is, $k_s \to \infty$. Then, continuous contact will occur when the radial coordinate is equal to the clearance between the rotor and the stator in the static configuration; that is $\rho = 1$ (or $\bar{\rho} = \delta$). Furthermore, synchronicity means that the angular coordinate is prescribed as

$$\gamma = \Omega\tau + \gamma_o. \tag{21}$$

The relative speed between the rotor and stator at the point of contact is then $v_{\text{rel}} = \Omega(R + \delta)$. Upon substituting Eq. (21) into Eqs. (12) and (13), the following equations are obtained

$$F_n = m_b\Omega^2 \cos\gamma_o + \Omega^2 - 1 \tag{22a}$$

$$2\zeta_b\Omega = -m_b\Omega^2 \sin\gamma_o - \mu F_n. \tag{22b}$$

Equations (22) contain two unknowns, namely γ_o and F_n. It is noted that F_n is a constraint force (like a Lagrange multiplier) that arises due to the contact constraint $\rho = \delta$. Equations (22) can be combined to solve for γ_o, which is given to be

$$\gamma_o = \arcsin\left(-\frac{2\zeta_b\Omega + \mu(\Omega^2 - 1)}{m_b\Omega^2\sqrt{1+\mu^2}}\right) - \phi, \tag{23}$$

where ϕ is the principal value of $\arctan(\mu)$. The forward whirling solution given by Eq. (21) will be valid provided that the argument of the arcsin function is bound in magnitude by unity. Thus, the condition for forward synchronous whirl is given to be

$$\left|-\frac{2\zeta_b\Omega + \mu(\Omega^2 - 1)}{m_b\Omega^2\sqrt{1+\mu^2}}\right| < 1. \tag{24}$$

Equation (24) is a necessary condition for the existence of forward synchronous whirl. Note that if this condition is true then there will be two values of γ_o that solve (23). As parameter values are varied and start to approach values for which condition (24) is violated, the two solutions coincide. Thus the equality in (24) gives the condition for a fold bifurcation at which a stable and an unstable state of forward synchronous whirl come together and are annihilated.

Note though that Eq. (24) is not a sufficient condition for forward synchronous whirl, because stator contact needs to be maintained. This condition is given by $F_n > 0$ where F_n is calculated from Eq. (22a) once γ_o has been determined. Passage of F_n through zero would represent a non-local qualitative change in which the motion lifts off from the constraint surface $\rho = \delta$.

It is intuitively clear that these considerations would still apply if the infinitely stiff stator is replaced with a large but finite value k_s. In particular, the lift-off condition would become a boundary equilibrium bifurcation in the terminology of non-smooth system analyses [13].

In what follows, Eqs. (24) and (22a) will be used to determine regions of synchronous whirl for the different friction models.

Figure 3 depicts regions of continuous-stator contact during forward synchronous whirl for the different friction models. Here, the Coulomb friction model and also the cubic models for which $\mu_s = 1.5\mu_m$ and three different values of v_m are considered. The dashed vertical black line in the figure is where the normal force F_n becomes positive, such that lift-off between rotor and stator would occur for all (μ,Ω) parameter values to the left of this curve. The shaded regions represent parameter regions of continuous forward whirling, given by the stable solution to Eq. (23). Note that there are two solutions of μ for a fixed value of Ω in Eq. (24), wherein one value of μ is positive and the other is negative. Here, the positive value of μ is the correct root, as the friction coefficient is assumed to be positive in the model development. Additionally, Eq. (24) yields solutions to the left of the vertical dashed line for the different friction models, which are non-physical since the normal force is of the wrong sign.

It is useful to compare the existence region for the different friction models. For lower values of Ω, the cubic friction model drops below the Coulomb contact line. This drop originates from the fact that $\mu_o > \mu_m$, and when Ω is small the effective friction is greater than μ_m. However, for the values of $v_m = 0.5, 0.25$, as Ω starts to increase, the region of contact increases until the boundary comes into contact with the Coulomb friction line, upon which the boundary starts to decrease. For the case of $v_m = 0.1$, the boundary region monotonically decreases to zero. This monotonic decrease occurs because the cubic friction for $v_m = 0.1$ reaches it's minimum value before the asymptotic. For all finite values of v_m, the boundary region will tend to zero in the limit of increasing Ω since $\mu \to \infty$ as $\Omega \to \infty$.

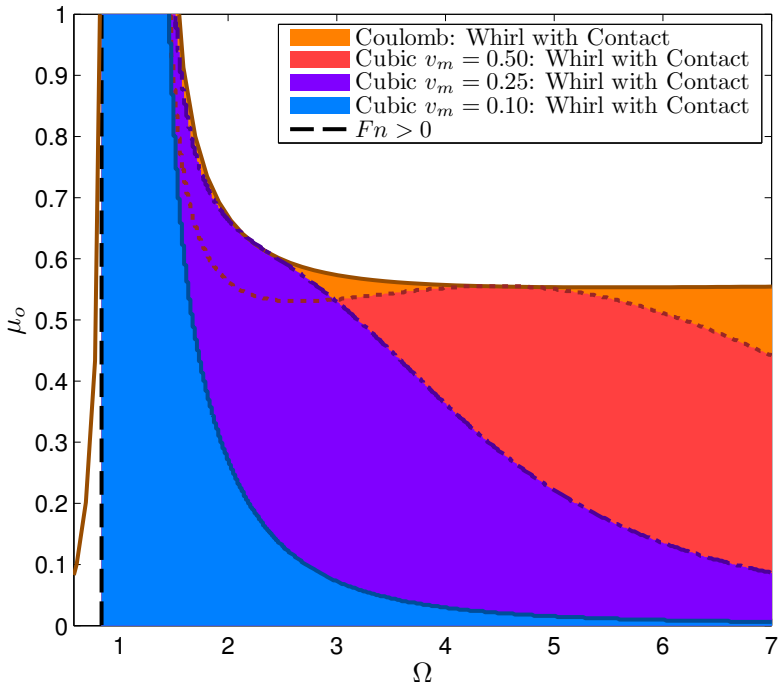

Figure 3: Stability regions during synchronous forward whirling for Coulomb and cubic friction ($\mu_m = \mu_o/1.5$).

A steady-whirl with contact solution does not exist in the white-shaded region to the top right of Figure 3. Within this region, simulations indicate that their is no stable contact forward whirling solution (not necessary synchronous), instead the rotor always loses contact with the stator. After a significant transient period the system settles into one of two other states, either free whirling (in the direction of drive rotation) without contact or self-excited backward whirling. Two of the typical responses, namely, free whirling and backward whirling are provided in Figure 4 for the parameter values of $\mu = 0.6$ and $\Omega = 2$. The trajectories of the rotor within the stator are shown in Figure 4(a), while the x and y time histories in Cartesian coordinates are shown in part (b) and the angular polar coordinate is shown in part (c). As shown in Figure 3, for this combination of μ and Ω, the rotor is also able to undergo forward whirl with stator contact. This brings to light the point that all of these three motions (forward whirl, backward whirl, and free whirl) are dependent upon the initial conditions. In the white shaded region to the left of the dashed line, the rotor will start free whirling or backward whirling (as shown later), depending on the initial conditions. It is noted that for the initial conditions and parameter ranges studied here, simulations did not reveal any other kinds of attractors. However, it is known that impacting motions, either periodic or chaotic, have been shown to occur in the past by [6, 7, 14] among others. Moreover, it is noted that for the relatively large δ used in the simulations, that the vertical dashed line (rotor-stator contact line) is relatively close to the first lateral natural frequency. For the parameter values selected here, the rotor will only make contact with the stator for large lateral displacements (cf. Figure 3 in [2]); however, the lateral resonance and contact line will separate for smaller values of δ, wherein the rotor will first make contact with the stator for small values of Ω.

3.2. Backward Whirling with Continuous Contact

Now the special case of backward whirling with continuous stator contact is addressed. The steady-state solution sought in this case is *pure stick motion*, which occurs when the relative speed between the rotor and stator is zero. This motion is also sometimes referred to in the literature as counter whirl, dry-friction whirl, or self-excited backward whirl.

In the current case, under the neglect of torsional deformations, the backward whirl region with pure stick is independent of the friction model and is only dependent upon the value of static friction when $v_{\text{rel}} = 0$. Under the assumption that the relative speed between the rotor and stator at the point of contact is zero, representing a pure stick condition, the whirl speed of the rotor can easily be derived from Eq. (17):

$$\dot{\gamma} = -\frac{R}{\delta}\bar{\Omega} \equiv -\omega$$

Here, the negative sign indicates that the rotor is whirling in the opposite direction to the drive rotation with angular speed Ω. Bartha [8] derived conditions for backward whirling with contact, under the assumption of negligible torsional deformation, eccentricity, or mass imbalance while the rotor is whirling at a constant angular speed ω in contact with an infinitely stiff stator. Taking those assumptions, force balance normally and radially at the boundary between slip and stick leads to

$$M\delta\omega^2 - \delta k_b = \bar{F}_n, \tag{25a}$$

$$\delta c_b \omega = \bar{F}_n \mu_o. \tag{25b}$$

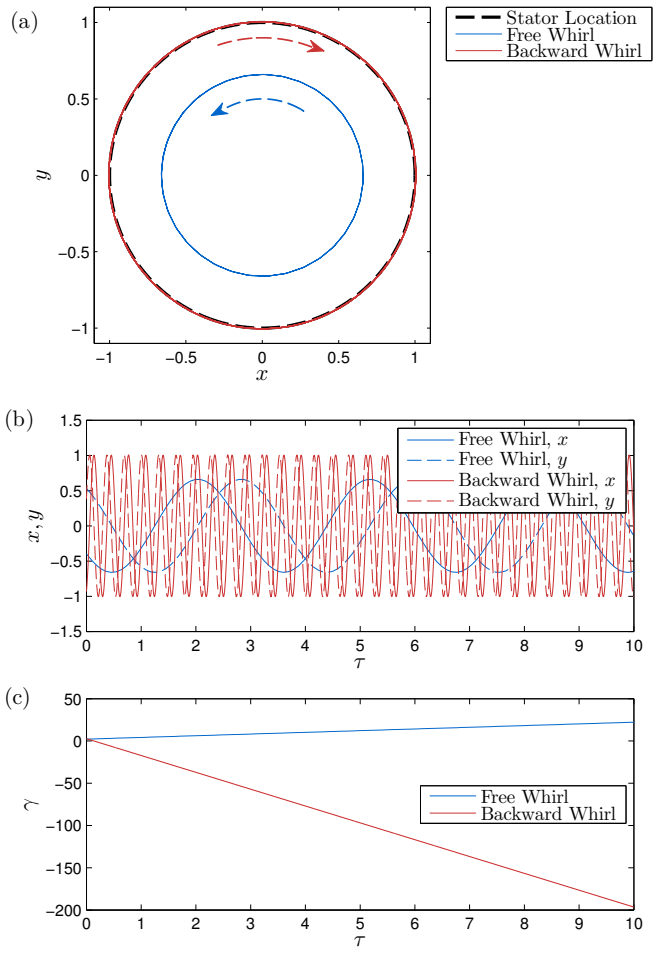

Figure 4: Typical responses for $\mu = 0.6$, $\Omega = 2$rad/s with Coulomb friction: (a) Rotor trajectory, (b) time histories of lateral displacement, and (c) angular polar coordinate γ.

Equation (25b) can then be substituted into (25a) in order to obtain the condition for the boundary between stick and slip; that is,

$$\omega_{\text{stick}}^2 - \frac{2\zeta\omega_n}{\mu_o}\omega_{\text{stick}} - \omega_n^2 = 0, \tag{26}$$

where $\omega_{n,b}$ is the first lateral natural frequency and ζ_b is the corresponding damping ratio

$$\omega_n = \sqrt{\frac{k_b}{M}}, \qquad \zeta = \frac{c_b}{2\sqrt{k_b M}}.$$

Equation (26) will yield two solutions for ω_{stick}. One solution will not satisfy Eqs. (25), while the other solution gives the condition for pure stick, $\mu < \mu_o$ or, equivalently

$$\omega > \omega_{\text{stick}} = \omega_n\left(\frac{\zeta}{\mu_o} + \sqrt{1 + \left(\frac{\zeta}{\mu_o}\right)^2}\right). \tag{27}$$

Equation (27) can also be expressed in terms of the non-dimensional drive speed as

$$\Omega > \frac{\delta}{R}\frac{\omega_n}{\omega_b}\left(\frac{\zeta}{\mu_o} + \sqrt{1 + \left(\frac{\zeta}{\mu_o}\right)^2}\right). \tag{28}$$

These approximate parameter regions of rotor-stator contact during backward whirl are plotted in Figure 5.

Note that in this approximate formulation, F_n is assumed to be constant during the motion. In practice, when non-vanishing eccentricity and mass imbalance are taken into account, the normal force will undergo oscillation about this nominal value due to the nonautonomous terms in equations (12), (13), and (14). Specifically, the normal force in equations (22a) will have a temporal dependence.

It should be noted that the regions shown in Figure 5 are strictly only relevant for finding regions of backward whirl (pure stick). In the red-shaded region, the rotor may in fact undergo forward synchronous whirling with or without stator contact. Rather than consider the effects of imbalance and eccentricity separately on these existence regions, we shall in the next section consider these effects in combination with torsional deformation.

4. Rotor-Stator Dynamics with Torsional Deformations

We now consider the effect of torsional deformation on the stability boundaries computed in the previous section. As before, forward whirling will be considered first, following by the case of backward whirling.

4.1. Forward Whirl with Torsional Deformations

Similar to case without torsional deformations we seek steady whirl solutions of the form

$$\theta = \theta_o \text{ and} \tag{29a}$$

$$\gamma = \Omega\tau + \gamma_o. \tag{29b}$$

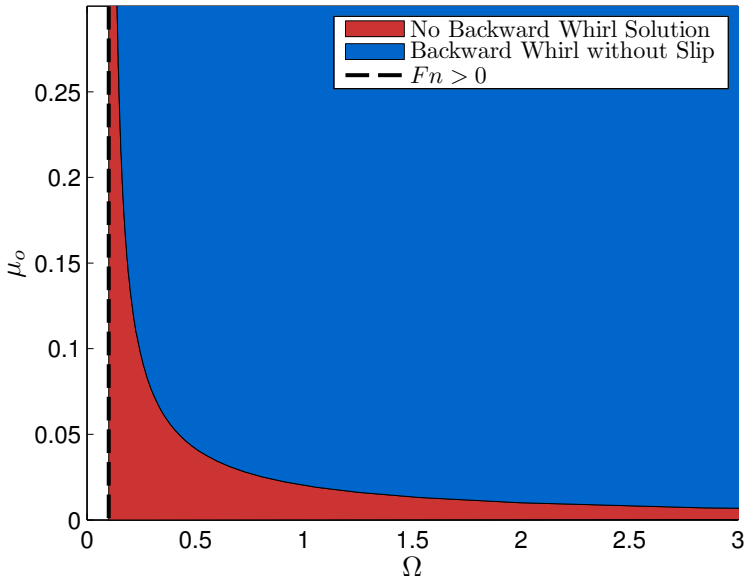

Figure 5: Approximate regions of pure stick and slip with rotor-stator contact under the assumption of negligible torsional deformations, mass imbalance, and eccentricity, given by solutions to Eq. (27).

Equations (29) can be substituted into Eqs. (12) and (13), while allowing $\rho = 1$. This leads to nonlinear equations that have to be solved for the unknown constants γ_o and θ_o:

$$\theta_o - \gamma_o = \arcsin\left(-\frac{2\zeta_b\Omega + \mu(\Omega^2 - 1)}{m_b\Omega^2\sqrt{1+\mu^2}}\right) - \phi, \tag{30a}$$

$$\frac{\omega_t^2}{\omega_b^2}\theta_o = -m_t\Omega^2\sin(\theta_o - \gamma_o) - m_f\mu\left[m_b\Omega^2\cos\psi + \Omega^2 - 1\right], \tag{30b}$$

where ϕ is again the principal value of $\arctan(\mu)$. In order to determine the stability of this solution, it is helpful to write

$$\gamma(\tau) = \hat{\gamma}(\tau) + \Omega\tau + \gamma_o \quad \text{and} \tag{31a}$$

$$\theta(\tau) = \hat{\theta}(\tau) + \theta_o, \tag{31b}$$

where the quantities with a carrot on top are assumed to be small perturbations to the steady whirl solution determined by Eqs. (30). Equations (31) can be substituted into Eqs. (12)-(14), and written in vector notation as

$$\hat{\mathbf{x}}' = \mathbf{F}_{\mathrm{FW}}(\hat{\mathbf{x}}), \tag{32}$$

where $\hat{\mathbf{x}}^T = \{\hat{\gamma}, \hat{\theta}, \hat{\dot{\gamma}}, \hat{\dot{\theta}}\}$ and the superscript T denotes the vector transpose operation. An explicit expression for $\mathbf{F}_{\mathrm{FW}}$ takes the form:

$$\mathbf{F}_{\mathrm{FW}} = \left\{ \begin{array}{c} \hat{\dot{\gamma}}, \\ \hat{\dot{\theta}}, \\ \begin{bmatrix} 1 & m_b(\mu \sin\psi + \cos\psi) \\ -m_t \cos\psi & 1 + \mu m_b m_f \sin\psi \end{bmatrix}^{-1} \left\{ \begin{array}{c} -2\zeta_t(\hat{\gamma}' + \Omega) + m_b(\Omega + \theta')\sin\psi - \mu F \\ -2\zeta_t\hat{\theta}' - \frac{\omega_t^2}{\omega_b^2}(\theta_o + \hat{\theta}) - m_t(\hat{\gamma}' + \Omega)^2 \sin\psi - m_f \mu F \end{array} \right\} \end{array} \right\}, \tag{33}$$

where

$$\psi = \gamma_o - \hat{\gamma} + \theta_o + \hat{\theta} \tag{34}$$

$$F = m_b(\Omega + \hat{\theta}')^2 \cos\psi + (\hat{\gamma}' + \Omega)^2 - 1 \tag{35}$$

The parameter regions in which steady forward-whirl solutions occur (γ_o, θ_o) occur, for two different values of torsional damping ζ_t is plotted in Figure 6. Note the similarity of these existence regions to those shown in Figure 3. Furthermore, for each equilibrium, the eigenvalues of $\mathbf{F}_{\mathrm{FW}}$ have been computed and give the conditions for instability. The yellow and green regions in Figure 6 depict parameter regions in which the equilibrium is unstable with complex conjugate eigenvalues. The boundary of this region represents a Hopf bifurcation. The yellow regions depicts where, during the ensuing torsional oscillations, the rotor looses contact with the stator (determined by $F_n < 0$). The green regions depict where the rotor stays in contact and undergoes limit cycle oscillations. As can be seen from Figure 6, increasing the torsional damping reduces the region where the rotor breaks contact with the stator.

One-parameter bifurcation diagrams corresponding to variation of Ω for fixed values of μ_o for the two cases shown in Figure 6(a) and (b) are shown in Figure 7(a) and (b). The results are computed numerically by direct integration; hence, only the stable motion branch is depicted. The results are shown in a Poincaré section corresponding to maxima of $\hat{\gamma}$. Figure 7(a), which is the case of no torsional damping is indicative of a supercritical Hopf bifurcation upon reduction of Ω. Additionally, inspection of the numerically computed eigenvalues, although not provided, indicate a Hopf bifurcation point. The limit cycle grows in amplitude upon further reduction of Ω until a point is reached for which $F_n < 0$ and the motion lifts off. A supercritical Hopf bifurcation is also observed in the case shown in Figure 7(b) for which $\zeta_t = 0.01$. As Ω is increased beyond the bifurcation point, a period-doubling bifurcation is observed before the rotor breaks contact with the stator.

Figure 8 presents similar results for the cubic friction model, taking specifically the case $\zeta_t = 0.1$ and $v_m = 1$. Looking at a one-parameter slice through the oval shaped region with $\mu_o \approx 0.1$ reveals another supercritical Hopf bifurcation, followed by a period doubling bifurcation before loss of contact ensues (results not shown). However, in the upper-left hand portion of Figure 8, there exists another region where torsional oscillations are present with rotor-stator contact. Here, the system still experiences a Hopf instability, but the amplitude of the oscillations are small.

4.2. Self-Excited Backward Whirling

Here, an exact contact condition will be sought including the combined effects of mass imbalance, eccentricity, and torsional deformation. As noted earlier, during backward self-exited

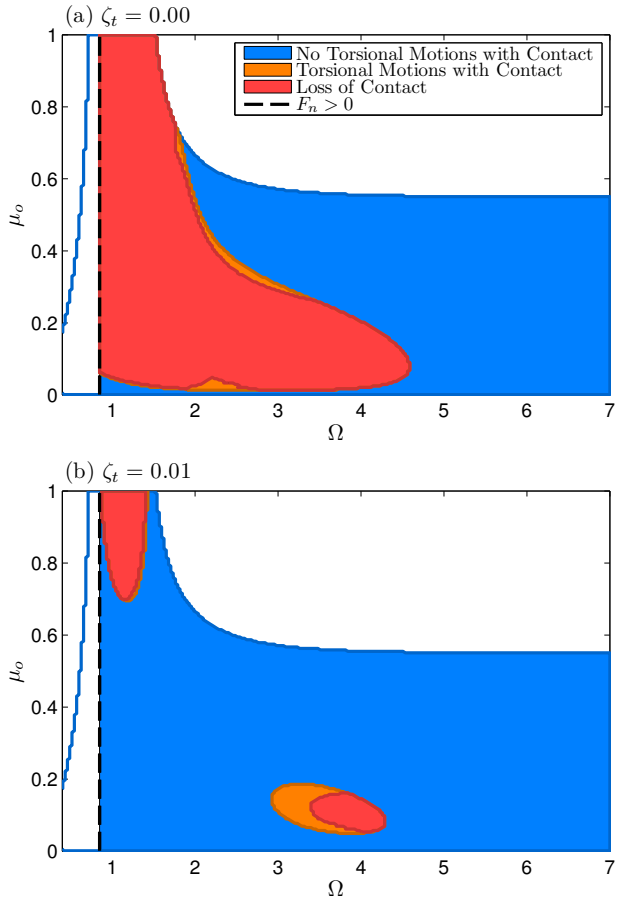

Figure 6: Parameter regions of existence and stability of synchronous forward whirling with torsional deformation in the case of Coulomb friction with (a) $\zeta_t = 0$ and (b) $\zeta_t = 0.01$.

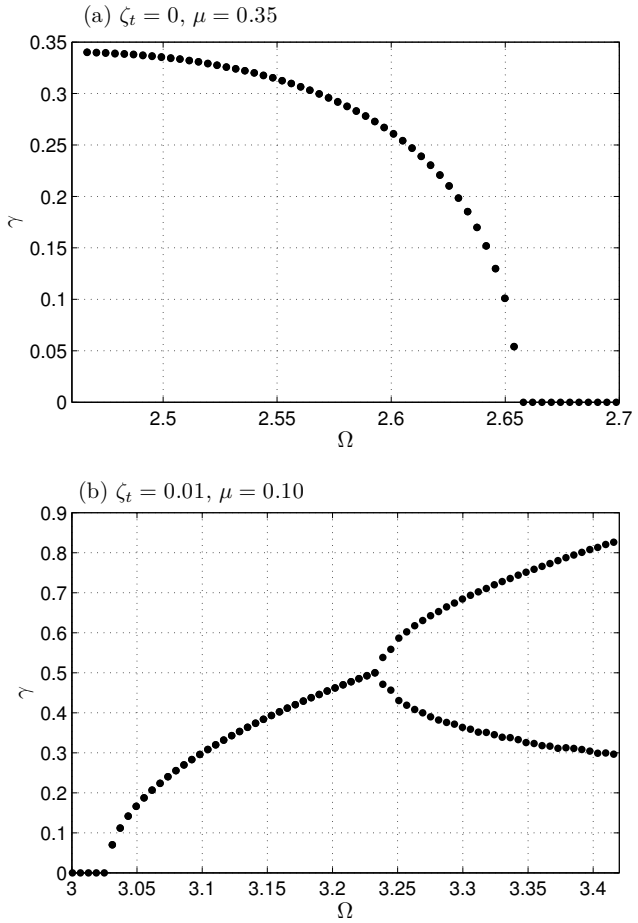

Figure 7: Bifurcation diagrams from sections taken from Figure 6 for (a) $\zeta_t = 0$, $\mu_o = 0.35$ and (b) $\zeta_t = 0.01$, $\mu_o = 0.10$.

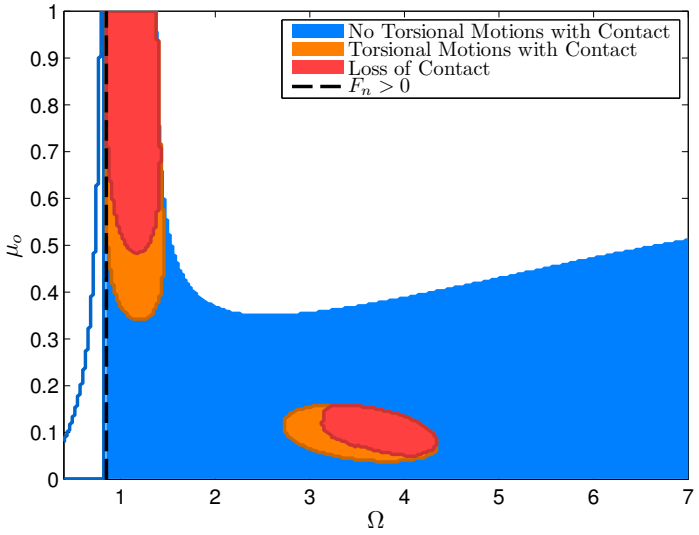

Figure 8: Regions of stability for cubic friction with parameters $\zeta_t = 0.01$, $v_m = 1$, and $\mu_m = \mu_o/1.5$.

whirl $\gamma' \approx -\frac{R}{\delta}\Omega$. However, an equation of the form

$$\gamma = -\frac{R}{\delta}\Omega\tau + \gamma_o, \tag{36}$$

where γ_o is a constant, can never satisfy Eq. (13) because of the mass imbalance and eccentricity terms. In order to search for non-equilibrium backward whirling solutions in this case, again the analysis considers the rigid limit by constraining the radial displacement such that $\rho = 1$. Perturbed quantities in γ and θ are sought of the form

$$\gamma = -\frac{R}{\delta}\Omega\tau + \hat{\gamma} \text{ and} \tag{37}$$

$$\theta = \hat{\theta}, \tag{38}$$

Upon substituting these relations into Eqs. (12), (13), and (14), the normal force F_n becomes a constraint force (like a Lagrange multiplier) which can be directly calculated from Eq. (12). The remaining two equations can be put into vector notation and may be compactly written as

$$\hat{\mathbf{x}}' = \mathbf{F}_{\mathrm{BW}}(\hat{\mathbf{x}}, \tau). \tag{39}$$

The equations (39) are then solved numerically to look for steady-state solutions for which the normal force remains positive. In numerically solving Eq. (39), Coulomb friction is applied under the approximation (20) with δ_f set to 1×10^8, and the relative tolerance of the Runge-Kutta numerical integrator was set to 1×10^{-8}. Studies were conducted by varying both of these quantities, and the chosen values were found to give sufficiently accurate results.

A summary of the results is given in Figure 9. For illustrative purposes, the line defining the boundary of backward whirling solution without torsional deformations and eccentricity, given

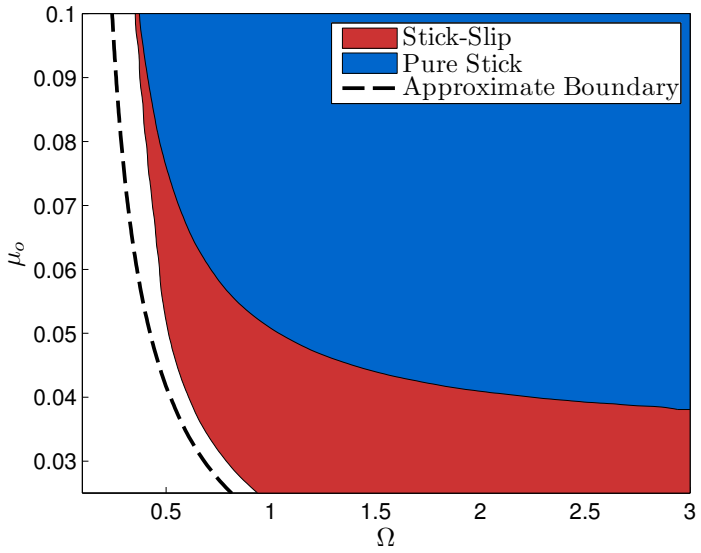

Figure 9: Regions of stick-slip and pure stick during backward whirling with torsional deformations. The dashed line represents the approximate contact boundary region given by Eq. (27).

by Eq. (27), is also provided in the figure. Note how this curve seems to underestimate the true minimum drive frequency for backwards whirl. If the friction coefficient μ_o is sufficiently small, then upon increasing Ω, there is a stick-slip oscillations before the rotor undergoes pure stick.

Typical solutions computed in each of the stick-slip and stick regions are shown in Figure 10. In both cases, the steady motion takes the form of a limit cycle. Note the distinction though that v_{rel} vanishes in the pure stick region, whereas there are time-intervals of non-zero v_{rel} for stick-slip. Also the limit cycle projected onto the $(\theta, \dot{\theta})$ phase plane is smooth in the slip region and non-smooth in the case of stick-slip. When simulating, the onset of the pure-stick region was determined when the relative speed v_{rel} became smaller than the solver tolerance. The left-hand boundary of the stick-slip region is defined by where lift-off occurs because a point on the limit-cycle has $F_n < 0$.

Looking again at Figure 9, note that this region of stick-slip vanishes for friction coefficients $\mu_o > 0.1$. For all higher μ_o-values, upon decreasing Ω, lift-off was found to occur directly within the pure stick region. For all friction values, it has been determined that the sticking solutions persist up to large Ω values. As Ω increases, the average value of torsional deformation θ becomes more and more negative to counterbalance the increased inertial forces, but the resulting amplitude of the limit cycle remains small.

5. Conclusion

Within this paper, the dynamics of a rotor with appreciable torsional deformations and stator contact have been analytically and numerically studied for both forward and backward whirling. In the case of forward whirling and negligible torsional deformations, an exact equation was derived to predict the regions where rotor stator contact exist. When including torsional deformations, a Hopf instability can arise and the rotor will whirl with torsional oscillations. Fur-

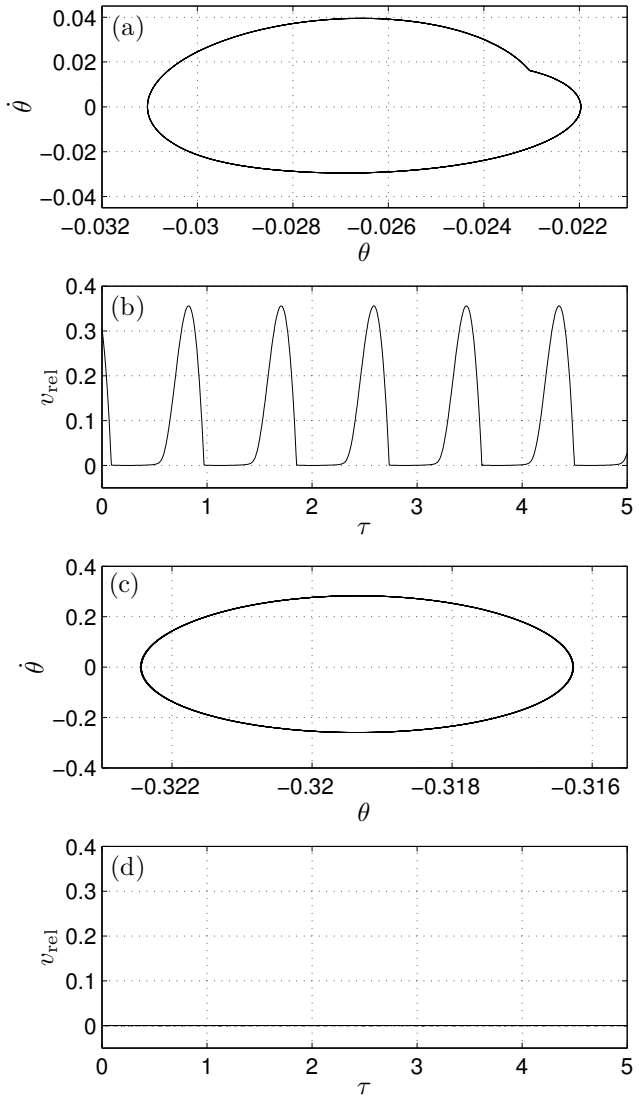

Figure 10: Stick-slip Motions ($\Omega \approx 0.66$,$\mu \approx 0.054$): (a) Phase diagram and (b) relative speed at the point of contact. Pure Stick ($\Omega \approx 7.98$,$\mu \approx 0.05$): (c) Phase diagram and (d) relative speed at the point of contact.

thermore, in certain regions the rotor response can exhibit a period doubling bifurcation. A key development here is to show that these oscillations can occur independently of the chosen friction model. This expands the analysis in [2] where the mechanism for Hopf bifurcation was found to be due to the negative slope in the cubic model. Note that the additional small amplitude limit cycles found in the upper left-hand portion of Figure 8 may well be related to those analyzed in the previous work [2].

In the second case of backward whirl with stator contact, we found evidence for transition between two types of motion, namely, stick-slip and pure stick motions. During stick-slip, the relative speed between the rotor and stator reaches zero for a finite amount of time, then slips free with positive relative speed. We have also shed light on the nature of the self-excited backward whirl, that it should represent periodic motion, rather than a radial equilibrium and that oscillation in both the torsional degree of freedom and relative angular position of the contact point must occur.

The findings within this work have applications to rotor systems with stator contact and large torsional deformations. Generally speaking, forward whirl, which represents pure slip motion occurs for smaller values of the friction coefficient, whereas backward whirl is likely to occur for sufficiently large friction. Note though, we find significant parameter regimes where both forward and backward whirl can coexist. Nevertheless, backward whirl appears somewhat more robust. Specifically, within the forward whirling regime, inclusion of a torsional degree of freedom can cause oscillations that quickly grow in amplitude so as to destroy the continuous contact. Also, small change in the details of the friction model or of torsional damping can cause significant differences to the existence and stability region of forward whirl. In contrast, we have found no evidence of instabilities during backward whirl other than at its small-Ω limit of existence. We also note how the analytic approximation (27) provides the correct trend for this lower rotation speed for backward whirl; however, this trend is a conservative estimate.

Acknowledgement

This work was supported by the EPSRC Programme Grant "Engineering Nonlinearity" EP/K003836/2. This work was partially supported by U.S. NSF Grant No. CMMI1436141.

References

[1] H. Jeffcott, The lateral vibrations of loaded shafts in the neighbourhood of a whirling speed - the effect of want of balance, Philosophical Magazine 37 (1919) 304–314.

[2] N. Vlajic, X. Liu, H. Karki, B. Balachandran, Torsional oscillations of a rotor with continuous stator contact, International Journal of Mechanical Sciences 83 (2014) 65–75.

[3] S. Edwards, A. Lees, M. Friswell, The influence of torsion on rotor/stator contact in rotating machinery, Journal of Sound and Vibration 225 (1999) 767–778.

[4] N. Mihajlovic, A. van Veggel, N. van de Wouw, H. Nijmeijer, Analysis of friction-induced limit cycling in an experimental drill-string system, ASME Journal of Dynamic Systems, Measurement, and Control 126 (2004) 709–720.

[5] N. Mihajlovic, N. van de Wouw, P. Rossielle, H. Nijmeijer, Interaction between torsional and lateral vibrations in flexible rotor systems with discontinuous friction, Nonlinear Dynamics 50 (2007) 679–699.

[6] F. Chu, Z. Zhang, Bifurcation and chaos in a rub-impact jeffcott rotor system, Journal of Sound and Vibration 210 (1998) 1–18.

[7] Z. Feng, X. Zhang, Rubbing phenomena in rotor-stator contact, Chaos, Solitons & Fractals 14 (2002) 257–267.

[8] A. Bartha, Dry Friction Backward Whirl of Rotors, PhD Thesis, Swiss Federal Institute of Technology, Zurich, Switzerland, 2000.

[9] D. Childs, A. Bhattacharya, Prediction of dry-friction whirl and whip between a rotor and a stator, Journal of Vibration and Acoustics 129 (2007) 355–362.
[10] X. Liu, N. Vlajic, X. Long, G. Meng, B. Balachandran, Nonlinear motions of a flexible rotor with a drill bit: stick-slip and delay effects, Nonlinear Dynamics 72 (2013) 61–77.
[11] N. Vlajic, X. Liu, H. Karki, B. Balachandran, Rotor torsion vibrations in the presence of continuous stator contact, ASME IMECE, DETC2012/MECH-89195 (2012).
[12] N. Vlajic, C.-M. Liao, H. Karki, B. Balachandran, Stick-slip motions of a rotor-stator system, Journal of Vibration and Acoustics 136 (2014) 021005.
[13] M. Bernardo, C. Budd, A. R. Champneys, P. Kowalczyk, Piecewise-smooth dynamical systems: theory and applications, volume 163, Springer Science & Business Media, 2008.
[14] E. V. Karpenko, M. Wiercigroch, M. P. Cartmell, Regular and chaotic dynamics of a discontinuously nonlinear rotor system, Chaos, Solitons & Fractals 13 (2002) 1231–1242.